

See discussions, stats, and author profiles for this publication at: <https://www.researchgate.net/publication/362961783>

A DFT+U approach to doped SrTiO₃ for solar harvesting applications

Article in Computational Materials Science · November 2022

DOI: 10.1016/j.commatsci.2022.111743

CITATIONS

0

READS

126

7 authors, including:



Shahrhan Ahmed Joy
University of Dhaka

7 PUBLICATIONS 12 CITATIONS

[SEE PROFILE](#)



Tarique Hasan Shushmoy
University of Dhaka

9 PUBLICATIONS 12 CITATIONS

[SEE PROFILE](#)



A. K. M. Sarwar Hossain Faysal
University of Dhaka

6 PUBLICATIONS 9 CITATIONS

[SEE PROFILE](#)



Sadiq Shahriyar Nishat
Rensselaer Polytechnic Institute

26 PUBLICATIONS 205 CITATIONS

[SEE PROFILE](#)

Some of the authors of this publication are also working on these related projects:



Effect of Rare Earth Substitution on the BaTiO₃ Based Ceramics [View project](#)



Fabrication and Characterization of Thin Films [View project](#)



Full length article

A DFT+U approach to doped SrTiO₃ for solar harvesting applications

Shahran Ahmed^a, Tarique Hasan^a, A.K.M. Sarwar Hossain Faysal^a, Sadiq Shahriyar Nishat^b,
M.N.I. Khan^c, Alamgir Kabir^d, Imtiaz Ahmed^{a,*}

^a Materials Science Research Laboratory, Department of Electrical and Electronic Engineering, University of Dhaka, Dhaka 1000, Bangladesh

^b Department of Materials Science and Engineering, Rensselaer Polytechnic Institute, Troy, NY, USA

^c Materials Science Division, Atomic Energy Centre, Dhaka 1000, Bangladesh

^d Department of Physics, University of Dhaka, Dhaka 1000, Bangladesh

ARTICLE INFO

Keywords:

SrTiO₃
Pt doped SrTiO₃
S doped SrTiO₃
Se doped SrTiO₃
DFT+U
HSE06

ABSTRACT

We present a Hubbard U optimized density functional theory based study of band gap engineered doped SrTiO₃ suitable for light sensitive applications. We tune the Hubbard U parameter U_{opt} to match the experimental direct band gap of SrTiO₃. We benchmarked the DFT+U_{opt} derived density of states, band structure and optical properties with that of sophisticated Heyd–Scuseria–Ernzerhof (HSE06) hybrid functional simulations. The reliability of the DFT+U method is further tested in simulating stability of the cubic SrTiO₃ from elastic tensor and density functional perturbation theory based phonon band structure calculations. Moreover, the DFT+U_{opt} simulated SrTiO₃ Raman peaks are identified against the experimental observations found in existing literature. We red shift the energy band gap of SrTiO₃ within the DFT+U_{opt} formalism from ultraviolet to visible range by incorporating different dopants such as Pt, S and Se which is consistent with recent HSE06 hybrid functional based simulations found elsewhere. The optical absorption simulations revealed steep absorption edges of doped SrTiO₃ in the visible spectrum. Overall, the DFT+U approach successfully probed the potential of doped SrTiO₃ in solar harvesting applications.

1. Introduction

Efficient absorption in visible range of the electromagnetic spectrum is one of the key requirements for solar harvesting applications, be it photovoltaic or photocatalytic [1,2]. The latter also requires the valence band maximum (VBM) and conduction band minimum (CBM) to be suitably aligned for driving redox reactions for water splitting [3]. Although the classic perovskite oxide strontium titanate SrTiO₃ (STO) has favourable band alignment, both its indirect (3.25 eV) and direct (3.75 eV) band gaps are in ultraviolet range which makes it a very inefficient absorber of visible electromagnetic radiation [4]. Hence tremendous efforts, both theoretical and experimental, have undergone to reduce the band gap of STO through doping which has been the holy grail to enhance its photo response in visible spectrum [5–8,8–12].

The key challenges in the STO band gap engineering through doping are (i) the introduction of shallow trap states near the band edges, (ii) controlling hybridization among dopants and host atoms to move the desired energy bands and (iii) keeping the non-magnetic nature of STO intact after doping [5–7]. To overcome these challenges, deeper understating about the behaviour of dopants can be facilitated from first principles calculations based on the density functional theory (DFT). The presence of 3d transition element Ti in STO dictates the

suitable dopants to have 3d, 4d or 5d orbitals in them. The reliable modelling of these localized orbitals with dilute Coulomb interaction usually requires sophisticated hybrid functional to produce accurate electronic and optical properties [1,13,14]. The inclusion of dopants also requires supercell approach containing considerable number of atoms to be incorporated in the DFT simulations. The hybrid functionals with STO supercell can put severe computational burden [15]. The Hubbard interaction corrected DFT+U formalism can be used as a possible alternative and have become popular in materials science community for its low computational cost [14,16–19]. The material dependent semi-empirical U parameter requires adhoc or parametric optimization for producing reliable estimates of different materials properties [14,19].

Recently, Mott insulating phase is discovered in doped thin film heterostructure containing STO [20–22]. In the Mott insulating phase, strong electron interaction requires an additional inter-site interaction V term in the Hubbard corrected DFT+U+V framework [23,24]. But here we focus on the bulk band insulating phase of cubic STO at room temperature. The DFT+U method has been widely used to study the behaviour of bulk insulating phase of STO, both pristine and with defects

* Corresponding author.

E-mail address: imtiaz@du.ac.bd (I. Ahmed).

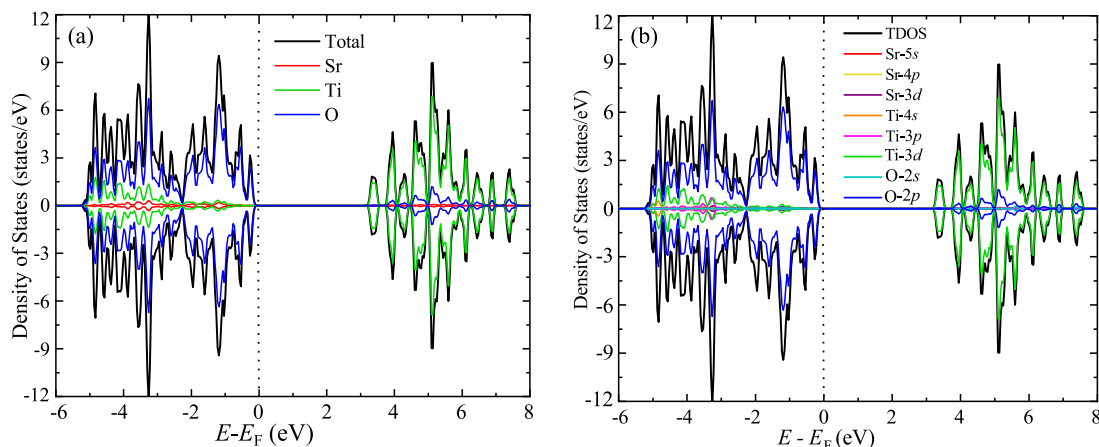


Fig. 1. Spin polarized total density of states (TDOS) and its projection onto (a) Sr, Ti and O atoms, (b) different orbitals in Sr, Ti and O for HSE06 functional.

such as vacancies and dopants [24–29]. The computational intense and reliable Heyd–Scuseria–Ernzerhof (HSE06) based simulations for doped STO can be found in Refs. [5–7,30]. The Sr atom helps to maintain the charge neutrality of the STO and have small contributions to electronic states of CBm and VBM. The co-doped STO involving combined Sr/Ti or Sr/O sites with multiple dopants have shown to modify the band gap of STO [31–34]. Since the electronic states near the CBm and VBM mainly originate from Ti-3d and O-2p orbitals, Ti and O sites have the potential to alter the properties of the STO significantly with monodoping techniques. Although several dopants from the transition and chalcogen elements apparently seem suitable, only few survive the test of undesirable charge trapping states and complications from dopant induced magnetic behaviour in STO [5–7]. Unfortunately, mono-doping can introduce localized acceptor or donor states in the band gap of STO due to charge mismatch between the host and dopant elements [6]. These trap states act as photo generated electron hole recombination centre and adversely affect the solar harvesting capabilities of STO [35,36]. Moreover, these uncompensated charged dopants favours formation of spontaneous charged vacancies in STO which may alter its non-magnetic nature. Hence we concentrate on isovalent dopants which lead to charge neutral defects formation in STO. Here we attempt to reproduce the sophisticated HSE06 simulation results obtained in Ref. [5] using computationally cheap DFT+U method. We tune the U on the Ti-3d in undoped STO to match the experimentally observed band gap of 3.75 eV. The density of states (DOS), electronic band structure and linear optical properties calculated from our DFT+U are benchmarked against that of HSE06 based simulations. We show that our tuned DFT+U is capable of producing reliable estimates of elastic, phonon vibrational spectrum, born charge mapping and Raman peak positions for undoped STO. Then we study the doped STO with three different dopants such as transition metal Pt and chalcogen elements S and Se, and show how they reduce the band gap of STO to visible spectrum making it an efficient absorber in solar harvesting applications.

2. Computational details

We performed the projector augmented wave (PAW) based spin-polarized simulations using the Vienna *Ab Initio* Simulation Package (VASP) [40,41]. The STO has 5 atoms (1 Sr, 1 Ti and 3 O) in its unit cell. We considered a $2 \times 2 \times 2$ supercell consisting of 40 atoms for all simulations presented in this article. The electronic configuration of STO is divided into valence and core to facilitate the PAW. We considered 10 electrons of Sr ($4s^2 4p^6 5p^2$), 10 electrons of Ti ($3p^6 3d^2 4s^2$) and 6 electrons of O ($2s^2 2p^4$) as valence electrons (in total 26 valence electrons) and the rest were modelled as frozen core. In cases of doped STO, we considered Pt- $5d^9 6s^1$, S- $3s^2 3p^4$ and Se- $4s^2 4p^6$ as valence

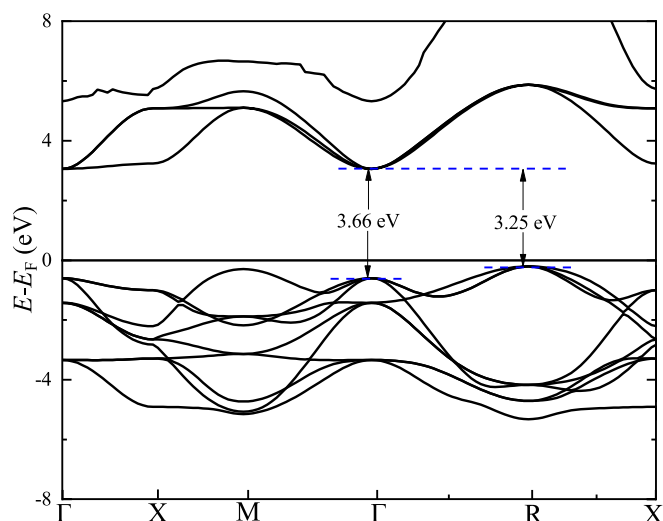


Fig. 2. Electronic band structure along high symmetry k-points Γ , R, X and M in the cubic STO Brillouin zone for HSE06 functional.

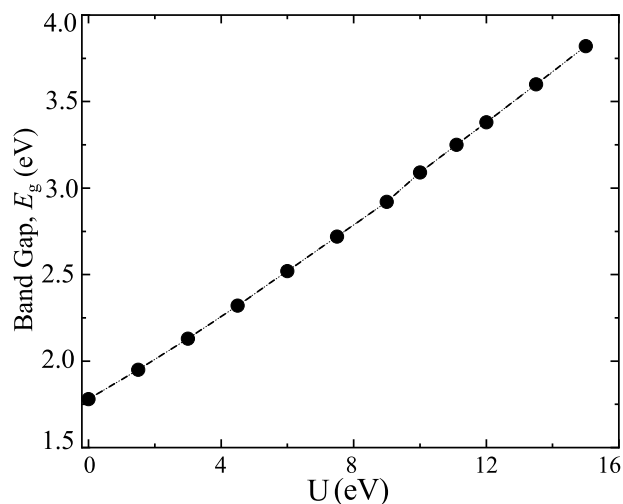


Fig. 3. The direct band gap E_g vs U applied on Ti-3d orbital.

Table 1

Crystallographic Parameters, Bond Angles, Bond Lengths and Band gap of STO for DFT+U, HSE06 and Experimental (Exp.) values to be found in Refs. [4,6,37–39].

Crystallographic Parameters, Bond Angles, Bond Lengths and Band gap									
DFT+U Simulation									
U (eV)	Lattice Parameter			Bond Lengths		Bond Angles			Band gap (eV)
	a=b=c (Å)	V (Å ³)	$\alpha = \beta = \gamma$ (°)	Sr-O (Å)	Ti-O (Å)	Sr-O-Sr (°)	Ti-O-Ti (°)	Sr-O-Ti (°)	
0	3.941	61.215	90	2.787	1.971	90, 180	180	90	1.78
1.5	3.951	61.679	90	2.794	1.976	90, 180	180	90	1.95
3	3.961	62.153	90	2.800	1.981	90, 180	180	90	2.13
4.5	3.971	62.630	90	2.808	1.986	90, 180	180	90	2.32
6	3.981	63.113	90	2.815	1.990	90, 180	180	90	2.52
7.5	3.992	63.600	90	2.822	2.022	90, 180	180	90	2.72
9.0	4.002	64.095	90	2.829	2.000	90, 180	180	90	2.92
10.5	4.008	64.428	90	2.835	2.004	90, 180	180	90	3.25
12	4.016	64.796	90	2.840	2.008	90, 180	180	90	3.38
13.5	4.022	65.100	90	2.844	2.011	90, 180	180	90	3.60
14.5	4.043	66.129	90	2.859	2.021	90, 180	180	90	3.82
HSE06	3.936	60.976	90	2.762	1.952	90, 180	180	90	3.66
Exp.	3.903	59.456	90	2.573	1.765	90, 180	180	90	3.75

electrons. We used $6 \times 6 \times 6$ Monkhorst Pack grid k-points mesh to sample the Brillouin zone (BZ). The structural relaxation are subjected to appropriate ionic (Hellmann–Feynman forces reached 0.001 eV/Å) and electronic convergences (self-consistent total energy convergence of 10^{-8} eV). The plane wave cut off was set to 680 eV in all simulations unless stated otherwise.

The computational accuracy of DFT simulations is sensitive to the choice of the functional used to model the electron interaction [15,42]. To model the electron interaction through the exchange–correlation in the Kohn–Sham Hamiltonian, we used two different functionals. The one is the DFT+U which uses the “Hubbard-U” scheme for Perdew–Burke–Ernzerhof (PBE) semi local generalized gradient approximation (GGA) [43–46]. The other is the sophisticated Heyd–Scuseria–Ernzerhof (HSE06) hybrid functional scheme where the GGA-PBE exchange interaction term is divided into short and long range parts, and the electron correlation part remain unaltered [47–49]. The exact Hartree–Fock exchange is used for the 25% of the short range GGA-PBE exchange with screening parameter $\mu = 0.2 \text{ \AA}^{-1}$ for the long range Coulomb potential. This empirical screening parameter defines the interaction range to be $2/\mu = 10 \text{ \AA}$ which is short ranged over a few neighbours at proximity [50]. The use of 25% Hartree–Fock exchange is well established from the perturbation theory [51,52]. Moreover the success of HSE06 functional in describing the *d* and *f* orbitals in oxides is ubiquitous in existing literatures [53–56]. For HSE06 electronic band structure (BS) simulations, we used the WANNIER90 tool to keep the computational burden manageable [5,14,57].

3. Electronic properties of STO

3.1. The HSE06 simulations

To understand the electronic properties of undoped STO, we simulated the spin-polarized total density of states (TDOS) within a 14 eV energy window centred at the Fermi level (E_F) for HSE06 functional as displayed in Fig. 1(a, b). The atomic density of states (DOS) confirms the dominance of O and Ti atoms in contributing to the electronic states near VBM and CBm respectively as displayed in Fig. 1(a). The O-2*p* states provide dominant contributions near the valence band maximum (VBM), whereas the conduction band minimum (CBm) is mainly populated by the Ti-3*d* states as shown in Fig. 1(b). The cation Sr²⁺ mainly donates electrons and their contributions near VBM and CBm are quite small [5]. For the electronic band structure (BS), we considered the high symmetry points Γ , R, X and M in the Brillouin zone (BZ) of the cubic STO within the energy range from -8 to 8 eV centred at E_F , see Fig. 2. The HSE06 produced band gaps of both direct (3.66 eV at Γ) and indirect (3.25 eV at R) nature which are in excellent agreement with the experimental observations of direct (indirect) band gap of 3.75 eV (3.25 eV) found in Ref. [4].

3.2. The DFT+U simulations

It is evident that Ti-3*d* significantly contributed to the CBm in STO. The semi-local GGA-PBE exchange–correlation is incapable of modelling localized Ti-3*d* orbitals. The excessive delocalization of Ti-3*d* orbital electrons by the semi-local GGA-PBE results in orbital instability [14]. This excess charge density delocalization is usually attributed to uncompensated electron self-interaction and improper modelling for non-local exchange interaction which leads to the well known band gap underestimation problem in DFT [53,58]. To overcome this, we tune the Hubbard U parameter in the DFT+U formalism to match the experimentally observed direct band gap of STO as shown in Fig. 3. The $U_{\text{opt}}=14.5$ eV in Ti-3*d* orbital produced a direct band gap of 3.83 eV which is closely matched with the experimentally obtained 3.75 eV in Ref. [4]. The structural relaxations were performed with different values of U and the lattice parameters for the relaxed structure are shown in Table 1. In case of U=0 eV, the GGA-PBE over-estimated the lattice parameters a, b, c as expected [59–61]. This overestimation grows with increasing value of U [62]. We observed 3.59% lattice parameter over-estimation at U = 14.5 eV as compared to the experimentally obtained values in Refs. [4,37,38]. We simulated the TDOS and its projections onto different atoms and orbitals with this optimized value of U_{opt} as shown in Fig. 5(a, b). The atomic and orbital DOS contributions of Sr, Ti, and O to VBM and CBm are similar to that of aforementioned HSE06. The DFT+U derived BS with U_{opt} is simulated in Fig. 6. Both CBm and VBM occur at the Γ point with a direct band gap of 3.83 eV. The direct nature of the band gap is more attractive for solar harvesting applications due to efficient light absorbing capabilities [1,2].

4. Optical properties of STO

The optical response characterized by the frequency dependent complex dielectric constant $\epsilon(\omega) = \epsilon_{\text{real}}(\omega) + i\epsilon_{\text{imag}}(\omega)$ ($i = \sqrt{-1}$, $\omega =$ angular frequency of the optical excitation) encodes the electronic properties of materials [63,64]. We estimated the dipole transition matrix elements from band structure simulations of both DFT+ U_{opt} and HSE06 functionals to calculate ϵ_{imag} using the Fermi’s golden rule [65–67]. The ϵ_{real} was derived from ϵ_{imag} using the standard Kramer–Kronig relations. The quantities like absorption coefficient α , reflectance R , energy loss function L , refractive index η , extinction coefficient K , and optical conductivity σ are obtained from the aforementioned ϵ which define the linear optical response [64]. Due to the cubic symmetry of the STO, the three orthogonal polarization along x, y and z directions denoted as E_x , E_y and E_z are equivalent with each others. We have not observed any optical anisotropy in the cubic STO as expected, hence all the optical parameters are averaged over the three polarizations

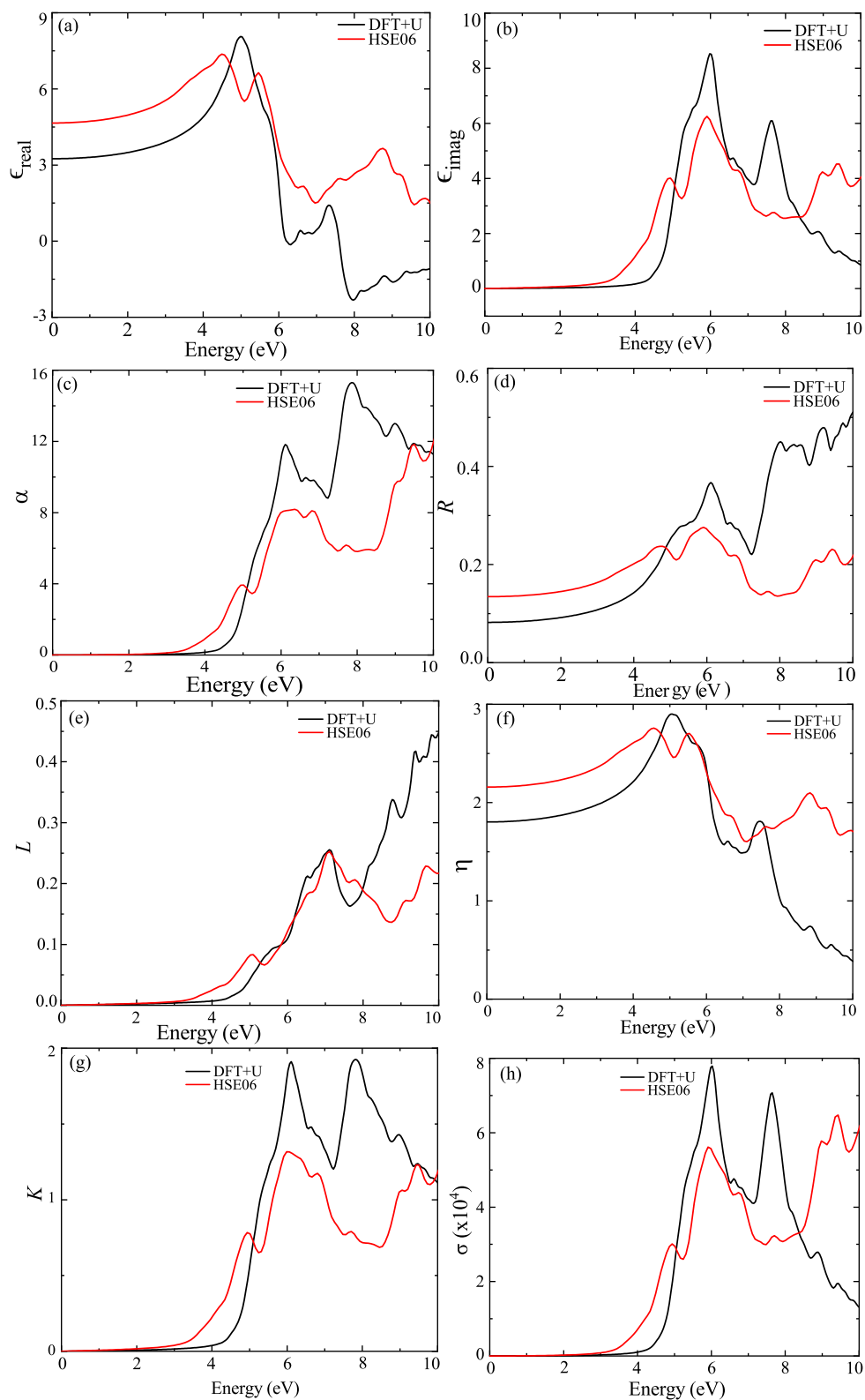


Fig. 4. Optical properties (a) real part of dielectric constant ϵ_{real} , (b) Imaginary part of the dielectric constant ϵ_{imag} , (c) Absorption coefficient α , (d) Reflectance R , (e) Loss function, L (f) Refractive index η , (g) Extinction coefficient K , (h) Optical conductivity σ as a function photon energy E averaged over three different polarization E_x , E_y and E_z calculated from DFT+ U_{opt} and HSE06 functionals.

E_x , E_y and E_z in Fig. 4. The value of the ϵ_{real} in the static limit $\omega \rightarrow 0$ are 3.24 and 4.63 as displayed in Fig. 4(a) for DFT+ U_{opt} and HSE06 functionals respectively. The first distinct summit peaks in ϵ_{real} for the two different functionals are quite close in energies (5.0 and

4.5 eV for DFT+ U_{opt} and HSE06 respectively). The energy cut-off E_{cut} (4.1 and 3.4 eV for DFT+ U_{opt} and HSE06 respectively) up to which the ϵ_{imag} stays zero matches with the estimated band gap for both functionals (3.83 eV for DFT+ U_{opt} and 3.66 eV in case of HSE06) as

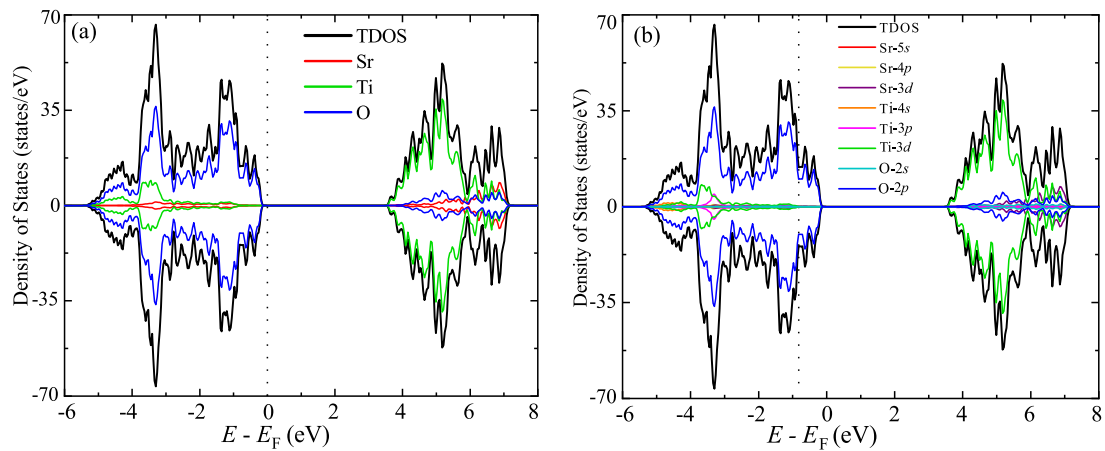


Fig. 5. Spin polarized total density of states (TDOS) and its projection onto (a) Sr, Ti and O atoms, (b) different orbitals in Sr, Ti and O for DFT+U with $U_{\text{opt}} = 14.5$ eV.

Table 2

Elastic constants (C_{ij}), bulk modulus (B_V , B_R and B_H), shear modulus (G_V , G_R , G_H), Young's modulus (E_V , E_R , E_H), Poisson ratio (ν_V , ν_R and ν_H) in Voigt–Reuss–Hill framework and Pugh ratio p_t for cubic STO using DFT, DFT+U and Experimental (Exp.) values to be found in Refs. [68,69].

Elastic Properties	Spin-Polarized						
	DFT	DFT+U (eV)					Exp.
		U=3	U=6	U=9	U=11	U=14.5	
C_{11} (GPa)	309.180	313.136	312.874	312.248	311.446	312.902	317.600
C_{12} (GPa)	94.084	93.373	89.981	87.019	85.281	85.254	102.500
C_{44} (GPa)	97.047	107.57	105.443	103.147	101.523	100.418	123.500
B_V (GPa)	165.783	166.235	164.282	162.103	160.674	161.137	174.200
B_R (GPa)	165.783	166.623	164.279	162.096	160.669	161.137	174.200
B_H (GPa)	165.783	166.627	164.279	162.096	160.669	161.137	174.200
G_V (GPa)	101.248	108.503	107.843	106.933	106.154	105.780	117.120
G_R (GPa)	100.991	108.487	107.765	106.736	105.851	105.383	116.584
G_H (GPa)	101.119	108.493	107.805	106.835	105.999	105.582	116.892
E_V (GPa)	252.367	267.454	265.453	262.97	260.974	260.367	287.033
E_R (GPa)	251.836	267.424	265.287	262.575	260.374	259.564	285.959
E_H (GPa)	252.102	267.436	265.367	262.775	260.673	259.966	286.536
ν_V	0.246	0.231	0.231	0.231	0.231	0.231	0.225
ν_R	0.247	0.233	0.233	0.233	0.233	0.231	0.266
ν_H	0.247	0.233	0.2331	0.230	0.231	0.231	0.226
p_t	0.610	0.649	0.658	0.658	0.661	0.655	0.672

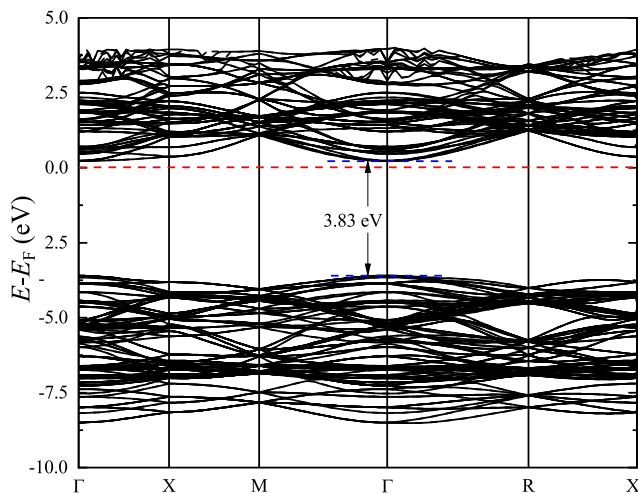


Fig. 6. Electronic band structure along high symmetry k-points Γ , X, M and Γ , R, X and M in the cubic STO Brillouin zone for DFT+U functional with $U_{\text{opt}} = 14.5$ eV.

shown in Fig. 4(b). The peaks in ϵ_{imag} defines the electronic transitions between different energy levels in STO and are in accord with the experimental observation in Ref. [81]. The DFT+ U_{opt} derived peak

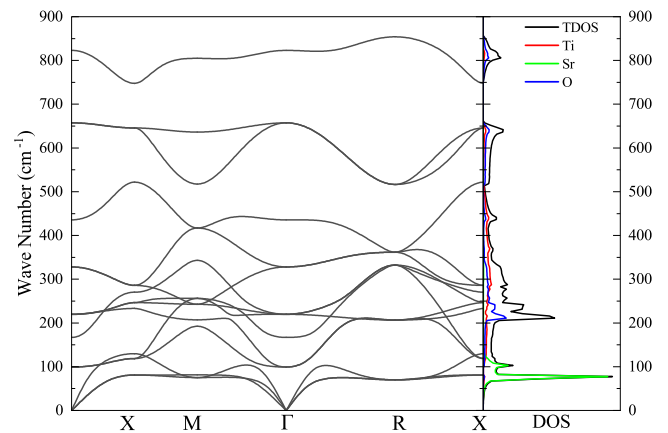


Fig. 7. Phonon band structure, total density of states TDOS and partial density of states PDOS for Sr, Ti and O atoms (in right column) using the DFPT of DFT+ U_{opt} functionals. The phonon dispersion curves in the band structure are plotted along the high symmetry k-points Γ , X, R, M in the STO BZ.

positions in energy, e.g. 5.3- and 6.0 eV, are in excellent match with that of 4.9- and 5.9 eV estimated from HSE06. The ϵ_{imag} defines the optical absorption α as depicted in Fig. 4(c). The α vanishes below

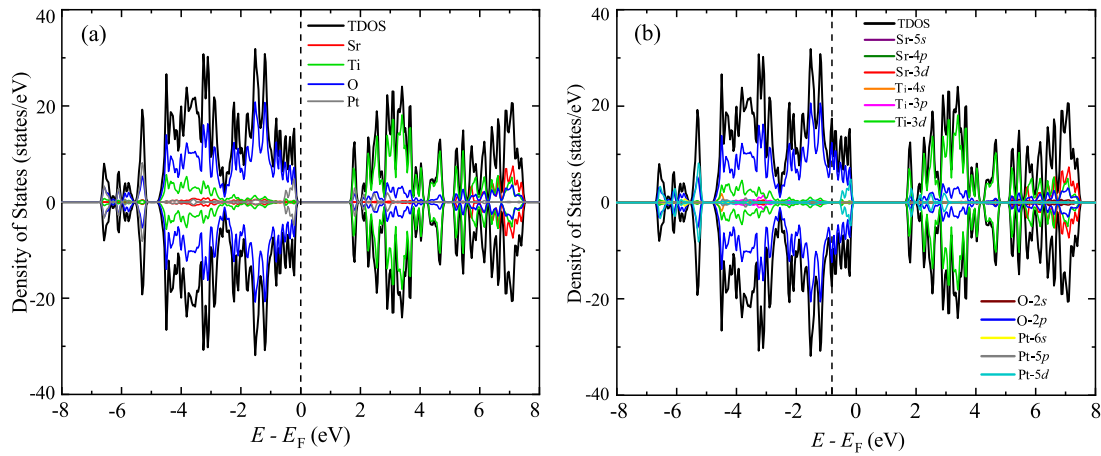


Fig. 8. Spin polarized total density of states (TDOS) and its projection onto (a) Sr, Ti, O and Pt atoms, (b) different orbitals in Sr, Ti, O and Pt for DFT+ U_{opt} functional.

Table 3

Calculated Born effective charge tensor of STO using DFT (GGA-PBE) and DFT+ U_{opt} .

Born Charge Analysis				
	Z_{Sr}^*	Z_{Ti}^*	$Z_{O_1}^*$	$Z_{O_2}^*$
GGA-PBE	+2.54	+6.32	-5.86	-2.02
DFT+ U_{opt}	+2.57	+4.47	-4.10	-1.87

Table 4

DFT+ U_{opt} simulated Raman peak positions in comparison with experimental observations to be found in Refs. [70–80].

Raman Peak Analysis		
Peak Assgn.	Theory (cm^{-1})	Experiment (cm^{-1})
TO ₁	130	127
LO ₁	173	176
TO ₂	178	178
TO ₂	194	197
2TA	220	205
TA+TO ₁	230	214
2TO ₁	240	223
LA+TA	260	277
TO ₁ +LA	270	282
2LA	300	296
TO ₁ +TO ₂	310	305
TO ₁ +TO ₂	315	320
TO ₂ +LA	340	336
LO ₁ +TO ₂	460	458
LO ₃	473	480
TO ₄	499	492
TO ₄	518	508
TO ₄	544	563
TO ₃ +LO ₁	600	604
LO ₂ +TO ₃	620	622
TA+TO ₄	630	630
TO ₁ +TO ₄	640	651
LO ₄	815	855
2LO ₂	946	903
2TO ₄	1038	950

the 3.5 eV for both functionals and rises beyond which are consistent with both theoretical and experimental observations in Refs. [5,81]. The DFT+ U_{opt} and HSE06 yield very similar optical reflectance R of 8% and 13% respectively in the static limit as shown in Fig. 4(d). The optical loss function L that defines the carrier mediated losses as a function of energy is plotted in Fig. 4(e). For both DFT+ U_{opt} and HSE06, the optical losses are vanishingly small below 3.5 eV which indicates the absence of optical carrier excitation. The simulated refractive index η is displayed in Fig. 4(f). In the $\omega \rightarrow 0$, both functionals provide good estimates for the η (1.8 and 2.16) which are in excellent

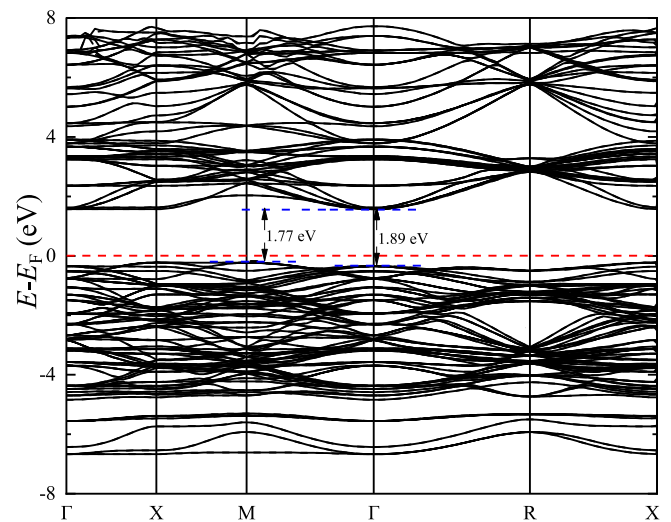


Fig. 9. Electronic band structure along high symmetry k-points Γ , R, X and M in the Pt doped STO Brillouin zone for DFT+ U_{opt} functional.

accord with the experimental observations in Ref. [81]. The extinction coefficient K in Fig. 4(g) vanishes below 3.5 eV as expected and shoots up beyond for both functionals. The optical conductivity $\sigma = \omega \epsilon_{imag}$ as shown in Fig. 4(h) shares similar features like the ϵ_{imag} displayed in Fig. 4(b). Overall, the DFT+ U_{opt} provides reliable estimates of optical properties which are consistent with HSE06 and experimental observations available in the literature.

5. Reliability of DFT+U

5.1. Elastic properties of STO

Now we test the applicability DFT+U in simulating the elastic properties of undoped STO. The structural stability was probed from elastic tensor C_{ij} calculations. The required finite lattice perturbations for the C_{ij} tensor estimation from standard strain–stress relationship were facilitated by applying appropriate forces along different directions [82, 83]. The 720 eV plane wave energy cutoff ensured the convergence of the stress tensor. The cubic STO embodies three independent non-zero elastic constants C_{11} , C_{12} and C_{44} . Based on these C_{ij} s, the necessary and sufficient Born criteria for mechanical stability for a cubic system

$$C_{11} > 0, C_{44} > 0, C_{11}^2 - C_{12}^2 > 0 \quad (1)$$

$$C_{11} - C_{12} > 0, C_{11} + 2C_{12} > 0, \quad (2)$$

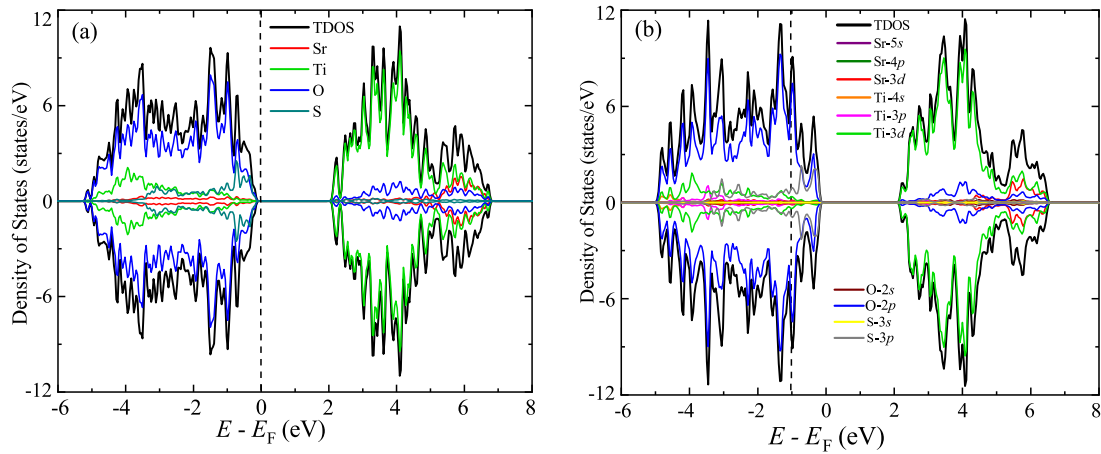


Fig. 10. Spin polarized total density of states (TDOS) and its projection onto (a) Sr, Ti, O and S atoms, (b) different orbitals in Sr, Ti, O and S for DFT+ U_{opt} functional.

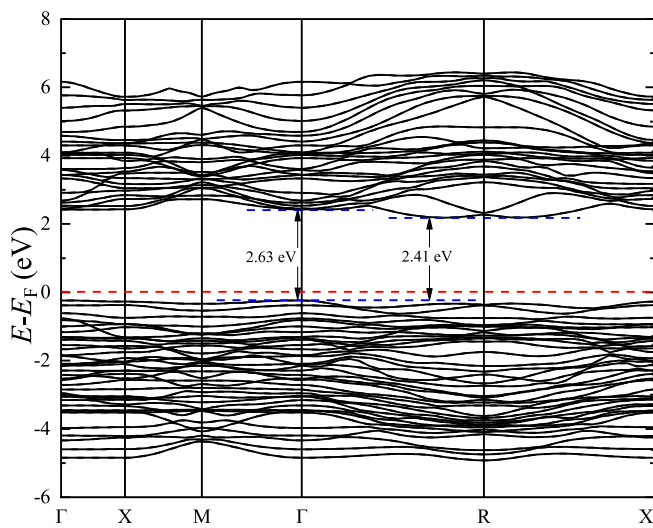


Fig. 11. Electronic band structure along high symmetry k-points Γ , R, X and M in the S doped cubic STO BZ for DFT+ U_{opt} functional.

are satisfied in both DFT (GGA-PBE) and DFT+U [84,85] for all values of U up to $U_{\text{opt}}=14.5$ eV, see Table 2. The other important elastic properties like bulk-modulus (B), shear modulus (G), Young's modulus (E), Poisson's ratio (ν) are calculated using three different theories such as Reuss (B_R , G_R , E_R and ν_R), Voigt (B_V , G_V , E_V and ν_V) and Hill (B_H , G_H , E_H and ν_H) [86–88]. The cubic symmetry of the STO unit cell resulted in same Voigt–Reuss–Hill bulk moduli as expected. The DFT functional gave smaller shear modulus ($G_H = 101.119$ GPa) and Young's modulus ($E_H = 252.102$ GPa) as compared to that of DFT+ U_{opt} . The DFT functional under binds the atoms in the unit cell and the U_{opt} corrects the binding energies to modify the G_H and E_H to 105.582 and 259.966 respectively. This implies enhancement of resistance to plastic deformation and stiffness in case of DFT+U functionals. Moreover, the estimated Poisson's ratio (ν_V , ν_R and ν_H) within the Voigt–Reuss–Hill framework, being smaller than the value of 0.33, corroborates the brittle nature of the STO. The STO brittleness was further confirmed as the estimated Pugh ratio (0.610 for DFT and 0.655 in case of DFT+ U_{opt}) stayed well below the critical value of 1.75. Overall, the DFT+ U_{opt} derived elastic properties are in good agreement with the experimental observations to be found in Refs. [68,69].

5.2. Phonon band structure of STO

The phonon dispersion defines vibrational and dynamical properties of materials [89]. Here we calculated the phonon dispersion and density of states (DOS) using density functional perturbation theory (DFPT) [90,91] along with the DFT+ U_{opt} functional. The full BZ was sampled with $6 \times 6 \times 6$ Monkhorst Pack grid k-points mesh without considering any symmetry restriction. The complete phonon vibrational spectrum consists of $d \times n = 15$ vibrational modes with $n = 5$ atoms (1 Sr, 1 Ti and 3 O) in the $d = 3$ dimensional cubic $Pm-3m$ STO unit cell. The low energy $d = 3$ acoustic modes in Fig. 7 are degenerate at the Γ -point [75–77]. The dynamical stability of the cubic STO is evident from the absence of any imaginary phonon frequencies in the entire BZ [80]. The $(d \times n) - 3 = 12$ optical modes (originated from irreducible representations of the $Pm-3m (O_h^1)$ space group) are also present at the Γ -point. Atoms with heavy (Sr), moderate (Ti) and light (O) masses are expected to dominate over lower, moderate and higher wave number ranges. This is evident as dominant contributions from Sr, Ti and O are in $50\text{--}150$ cm^{-1} , $150\text{--}300$ cm^{-1} and $250\text{--}550$ cm^{-1} wave number ranges respectively, as displayed in the right column of Fig. 7.

5.3. Born charge of STO

The Born effective charge (BEC) bear the signature of screened Coulomb interaction among the nuclei which play an important role in controlling the lattice dynamics and phonon dispersion [92,93]. The BEC encodes the charge dynamics in response to perturbation in atomic positions [94–96]. We calculated the BEC tensor for both DFT (GGA-PBE) and DFT+ U_{opt} , and displayed the values in Table 3. The Sr and Ti atoms have isotropic charge tensors due to the spherical symmetry at their atomic sites, whereas the O atom having local tetragonal symmetry needs two independent elements O_{\perp} (displacement perpendicular to Ti-O bond) and O_{\parallel} (displacement parallel to Ti-O bond). Hence for the cubic STO, 4 independent numbers Z_{Sr}^* , Z_{Ti}^* , $Z_{O_{\parallel}}^*$ and $Z_{O_{\perp}}^*$ are sufficient. The nominal charges of Sr, Ti and O are defined by their +2, +4 and -2 valence states in a closed shell ionic picture where Sr and Ti are electron donors and O acts as electron acceptor. The GGA-PBE and DFT+ U_{opt} resulted Z_{Sr}^* of +2.54 and +2.57 respectively, which are close to the nominal static +2 charge of Sr atom. For the $Z_{O_{\perp}}^*$, the GGA-PBE produced (-2.02) excellent match with static -2 charge of the O ion. The U interaction term shifted the $Z_{O_{\perp}}^*$ (-1.87) slightly away from -2 but pushes the Z_{Ti}^* (+4.47) quite close to the nominal static +4 charge state. The U_{opt} also reduces the anomaly in $Z_{O_{\parallel}}^*$ from -5.86 to -4.10 . The presence of these Born charge anomalies can result from the hybridization of Ti-3d and O-2p [96,96,97]. The hybridization allows charge delocalization (aids covalency and weakens the ionic

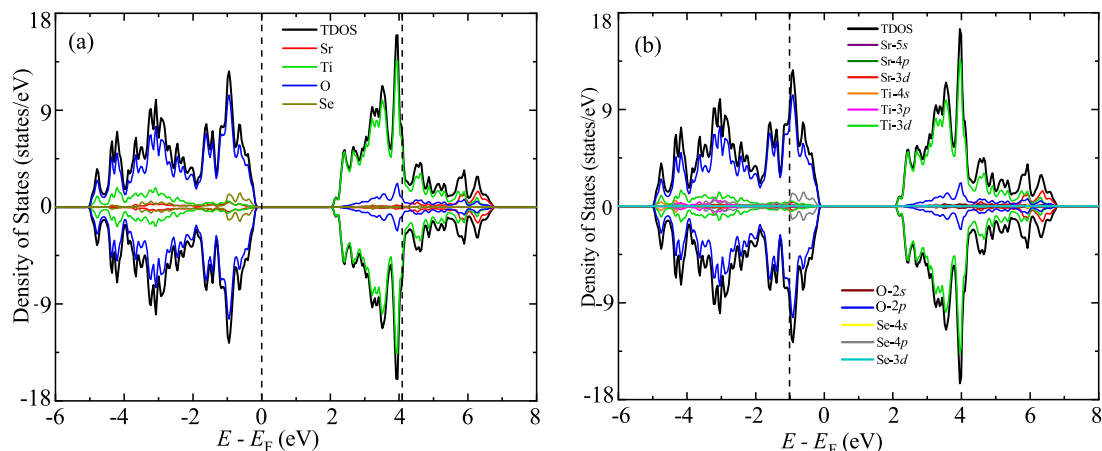


Fig. 12. Spin polarized total density of states (TDOS) and its projection onto (a) Sr, Ti, O and Se atoms, (b) different orbitals in Sr, Ti, O and Se for DFT+ U_{opt} functional.

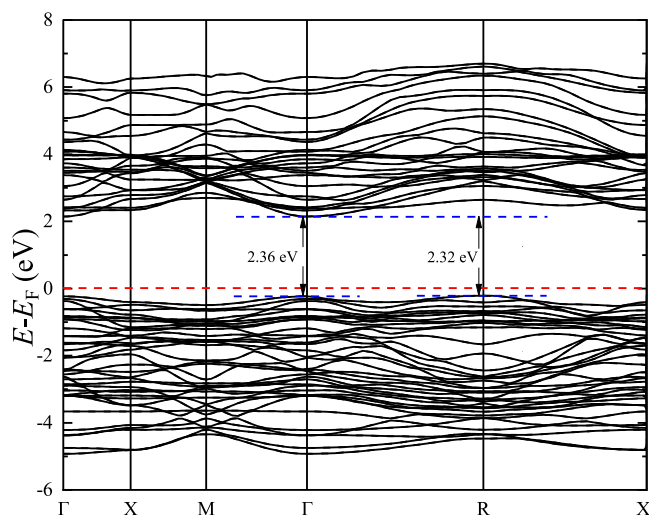


Fig. 13. Electronic band structure along high symmetry k-points Γ , X, M and Γ in the Se doped cubic STO BZ for DFT+ U_{opt} functional.

nature of Ti-O) resulting in dynamic contribution superimposed on the nominal charges [98]. The U_{opt} term added to Ti-3d orbital affects the degree of hybridization which in turn controls the dynamic nature of the BEC [93].

5.4. Raman peaks of STO

Raman spectra probes the symmetry and structure of the underlying crystal. We simulated the Raman peak positions for the DFT+ U_{opt} functional and benchmarked them in Table 4 against the available experimental observations in Refs. [70–80]. Depending on the temperature, STO exists in two different phases i.e., cubic $Pm-3m$ (~ 300 K) and tetragonal (~ 97 K). In the high temperature para-electric phase, among the triply degenerate $15 3F_{1u} + F_{2u}$ modes, both F_{1u} and F_{2u} are Raman inactive (cubic symmetry forbids the first order Raman scattering) [75–80]. The second order two photon processes dominate the Raman scattering. In the low temperature tetragonal $P4$ mm phase, the mode splitting occurs where F_{1u} generates E (doubly degenerate) and A_1 (non-degenerate), and F_{2u} splits into E and B_1 modes. All A_1 , E and B_1 are Raman active which characterize the Raman modes as $\Gamma_{Raman} = 3(A_1 + E) + E + B_1$. The presence of long-range electrostatic interaction provide further splitting of A_1 and E modes into TO and LO Raman modes. We observed a number of forbidden first-order Raman

modes denoted by TO_m and LO_m at 130, 170, 180, 190, 473, 520, 544, 815 cm^{-1} which are in good agreement with the experimental observations. The simulated two photon processes denoted by LA+TA, TA+ TO_m , LA+ TO_n , LO_m + TO_n , $2LO_m$ and $2TO_m$, which describe the second order Raman scattering, are also closely matched with the experiments [70–80].

6. Electronic band gap engineering of STO for solar harvesting

We have considered three different dopants such as Pt, S and Se which have the potential to suitably tune the band gap as per the Ref. [5]. We performed DFT+ U_{opt} simulations to probe the electronic and optical absorption properties desired in solar harvesting applications.

6.1. Pt doped STO

We replaced the 3d-TM Ti with 5d-TM Pt in case of the Pt-doped STO. The Pt atom donated 4 electrons and attained non-magnetic Pt^{4+} configuration. The 6 electrons in the 5d orbitals of Pt^{4+} occupied the low lying three fold degenerate t_{2g} states leaving the two-fold degenerate e_g levels empty. The atomic DOS confirms the contribution of the Pt atom in VBM as per Fig. 8(a). Significant amount of mixing occurs between O-2p and Pt-5d at the VB; whereas near the bottom CB hybridization occurs among O-2p, Pt-5d and Ti-3d as shown in Fig. 8(b). This is consistent with the HSE06 DOS simulations in case of Pt-doped STO to be found in Ref. [5]. The electronic BS simulations revealed a significant band gap reduction as displayed in Fig. 9. The global VBM and CBM occurred at M and Γ points respectively giving rise to 1.77 eV indirect band gap. This indirect nature is consistent with the HSE06 simulations present in the Supplementary Information of Ref. [5]. The VB dispersion is not significant and at the Γ -point the direct band gap is turned out to be 1.89 eV.

6.2. S doped STO

The chalcogen S replaces the O atom in STO due to comparable ionic radii and isovalence considerations. The S atom originates DOS in the VBM as depicted from the atomic DOS projection in Fig. 10(a). Similar S atomic DOS can be found in Ref. [5] derived from HSE06 simulations. The hybridization occurs among O-2p and S-3p near the top of the VBM as can be seen from the DFT+ U_{opt} DOS simulation in Fig. 10(b) and reduces the energy band gap around E_F . From the BS simulation in Fig. 11, it is evident that the global CBM and VBM are in $\Gamma \rightarrow R$ and Γ respectively, which defines an indirect band gap of 2.41 eV. In contrast, the HSE06 simulation results in a CBM at the Z point [5]. At the Γ point the direct band gap is found to be 2.63 eV which is an overestimation of the HSE06 derived band gap of 2.4 eV in Ref. [5].

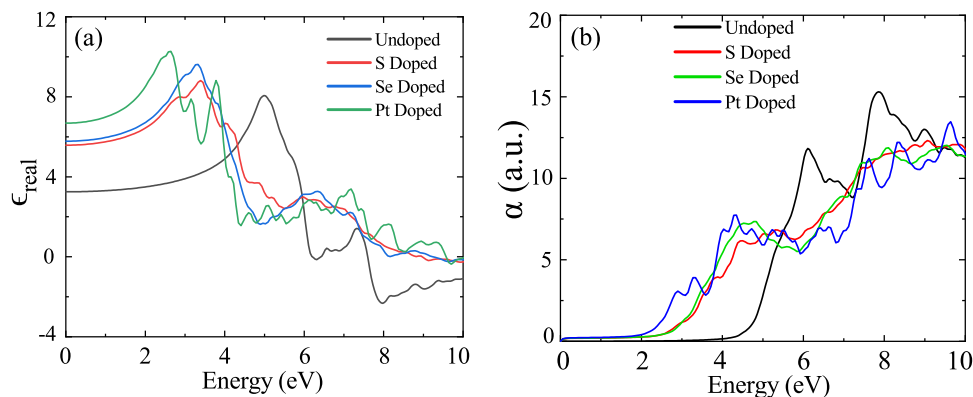


Fig. 14. Optical properties. (a) Real part of dielectric constant ϵ_{real} , (b) Absorption coefficient α as a function photon energy E for undoped, Pt, S, and Se doped STO averaged over three different polarization E_x , E_y and E_z calculated from DFT+ U_{opt} .

Table 5

Effective mass of electron (m_e^*) and hole (m_h^*) in the units of free electron mass m_0 along $\Gamma \rightarrow M$ and $\Gamma \rightarrow R$ for undoped, Pt-, S- and Se-doped STO using DFT+ U_{opt} .

Carrier Effective Mass			
Material	k-path	m_e^*	m_h^*
STO	$\Gamma \rightarrow M$	1.081	-0.918
	$\Gamma \rightarrow R$	0.884	-0.859
Pt-doped STO	$\Gamma \rightarrow M$	0.895	-2.847
	$\Gamma \rightarrow R$	0.453	-2.238
S-doped STO	$\Gamma \rightarrow M$	1.322	-4.185
	$\Gamma \rightarrow R$	3.751	-0.888
Se-doped STO	$\Gamma \rightarrow M$	0.539	-0.936
	$\Gamma \rightarrow R$	1.432	-2.359

6.3. Se doped STO

In case of Se-doped STO, the Se atom formed atomic DOS near the VBM as shown in Fig. 12(a), which is consistent with the HSE06 simulations in Ref. [5]. The Se dopants, as it replace O atoms in the STO unit cell, provide orbital mixing between O-2p and Se-4p at the top of the VB as depicted in Fig. 12(b) and shrinks the energy band gap to the visible range. The simulated BS in Fig. 13 revealed the CBm and VBM to occur at the Γ point with a direct band gap of 2.36 eV which is an over estimation of 2.16 eV direct band gap obtained from HSE06 in Ref. [5]. The presence of a second local VBM at point R gives an indirect band gap of 2.32 eV. A similar local VBM can be seen at Z point with an indirect band gap of ~ 2.16 eV for HSE06 simulations in Ref. [5].

7. Optical absorption

Now we calculate linear optical properties in cases of Pt-, S- and Se-doped STO and compared them with that of the undoped STO in Fig. 14. In the static $\omega \rightarrow 0$ limit, the ϵ_{real} is increased with the incorporation of dopants S (5.5), Se (5.8) and Pt (6.7) as compared to undoped STO (3.28) as displayed in Fig. 14(a). The peak of the undoped STO is shifted toward low energies due to the presence of dopants. The optical absorption spectrum of Pt-, S- and Se-doped STO are superimposed on that of undoped STO in Fig. 14(b). The optical absorption α rises from zero at threshold energies of 1.91-, 2.47- and 2.29 eV for Pt-, S- and Se-doped STO respectively which are much lower than that of undoped STO (3.81 eV). The steep absorption edges shifted to visible spectrum in all three doped STO cases as compared to the one in UV range for the undoped STO.

8. Effective mass

The effective mass of the charge carriers like electrons (m_e^*) and holes (m_h^*) inside a material are derived from the band curvature near the CBm and VBM respectively [99,100]. The band curvature can be obtained by parabolic fitting of the CBm and VBM [1]. The m_e^* and m_h^* for undoped, Pt-, S- and Se-doped STO are calculated using DFT+ U_{opt} and displayed in Table 5. The relevant k-paths are chosen to be $\Gamma \rightarrow M$ and $\Gamma \rightarrow R$ from the cubic symmetries of the band structure calculations. In case of undoped STO, the $m_e^* = 1.08m_0$, $0.884m_0$ and $m_h^* = -0.918m_0$, $-0.859m_0$ are in good agreement with that of Ref. [101]. For Pt-doped STO, the $m_e^* = 0.453m_0$ is below the $0.5m_0$ along $\Gamma \rightarrow R$ which is desired in solar harvesting applications [1]. The $m_e^* = 3.751m_0$ ($\Gamma \rightarrow R$) and $m_h^* = -4.185m_0$ ($\Gamma \rightarrow M$) in case of S-doped STO resemble effective mass enhancement due to doping [102]. In case of Se-doped STO, the $m_e^* = 0.539m_0$, being close to $0.5m_0$ along $\Gamma \rightarrow M$ can favour efficient photo generated carrier separation.

9. Conclusion

We tuned the Hubbard U parameter in DFT+ U formalism and matched the electronic and optical properties of undoped STO to those derived from the HSE06 functional. The optimum U_{opt} produced reliable estimates for (i) structural stability from the stress tensor, (ii) dynamic stability from DFPT based phonon structure, (iii) born charge tensor and (iv) Raman peak positions in case of undoped STO. We used the DFT+ U approach for studying the doped STO with three different dopants such as Pt, S and Se; and have shown to red shift the direct band gaps to 1.89-, 2.63- and 2.36 eV respectively, all of which are in the visible range of the electromagnetic spectrum. Notably, these dopants kept the non-magnetic nature of the STO intact and no impurity states or charge trapping centres were introduced within the band gap. Overall, the computationally cheap DFT+ U successfully probed the applicability of doped STO in solar harvesting applications.

CRediT authorship contribution statement

Shahran Ahmed: Performed the DFT+ U simulations. **Tarique Hasan:** Performed the DFT+ U simulations. **A.K.M. Sarwar Hossain Faysal:** Performed the DFT+ U simulations. **Sadiq Shahriyar Nishat:** Helped S.A. in HSE06 simulations. **M.N.I. Khan:** Performed the DFT+ U simulations. **Alamgir Kabir:** Performed the DFT+ U simulations. **Imtiaz Ahmed:** Planned, managed and supervised the entire project, Performed the DFT+ U simulations, Performed the data analysis, Wrote the article.

Declaration of competing interest

The authors declare that they have no known competing financial interests or personal relationships that could have appeared to influence the work reported in this paper.

Data availability

Data will be made available on request.

Acknowledgements

I.A. gratefully acknowledges support from Special Allocation for Science and Technology 2021–2022, Bangladesh (Code: EAS495), Ministry of Science and Technology, Government of the People's Republic of Bangladesh and Centennial Research Grant (CRG 2021–2022), University of Dhaka, Bangladesh. We are also very thankful to Dr. Shafiul Alam, Department of Electrical and Electronic Engineering, University of Dhaka and Dr. Md. Mosaddek Khan, Department of Computer Science and Engineering, University of Dhaka for their persistent support. All simulations were performed in the high performance computing facility provided by Bangladesh Research and Education Network (BdREN). We gratefully acknowledge ample and graceful computational support from BdREN.

References

- [1] T. Le Bahers, M. Rerat, P. Sautet, Semiconductors used in photovoltaic and photocatalytic devices: assessing fundamental properties from DFT, *J. Phys. Chem. C* 118 (12) (2014) 5997–6008.
- [2] R.R. Lunt, T.P. Osedach, P.R. Brown, J.A. Rowehl, V. Bulović, Practical roadmap and limits to nanostructured photovoltaics, *Adv. Mater.* 23 (48) (2011) 5712–5727.
- [3] Y. Gai, J. Li, S.-S. Li, J.-B. Xia, S.-H. Wei, Design of narrow-gap TiO₂: a passivated codoping approach for enhanced photoelectrochemical activity, *Phys. Rev. Lett.* 102 (3) (2009) 036402.
- [4] K. Van Benthem, C. Elsässer, R. French, Bulk electronic structure of SrTiO₃: Experiment and theory, *J. Appl. Phys.* 90 (12) (2001) 6156–6164.
- [5] Y. Hou, S. Ardo, R. Wu, Hybrid density functional study of band gap engineering of SrTiO₃ photocatalyst via doping for water splitting, *Phys. Rev. Mater.* 5 (6) (2021) 065801.
- [6] B. Modak, S.K. Ghosh, Enhancement of visible light photocatalytic activity of SrTiO₃: A hybrid density functional study, *J. Phys. Chem. C* 119 (41) (2015) 23503–23514.
- [7] M. Kumar, P. Basera, S. Saini, S. Bhattacharya, Role of defects in photocatalytic water splitting: Monodoped vs Codoped SrTiO₃, *J. Phys. Chem. C* 124 (19) (2020) 10272–10279.
- [8] C. Wang, H. Qiu, T. Inoue, Q. Yao, Band gap engineering of SrTiO₃ for water splitting under visible light irradiation, *Int. J. Hydrog. Energy* 39 (24) (2014) 12507–12514.
- [9] S.W. Bae, P.H. Borse, J.S. Lee, Dopant dependent band gap tailoring of hydrothermally prepared cubic SrTi_{1-x}M_xO₃ (M=Ru, Rh, Ir, Pt, Pd) nanoparticles as visible light photocatalysts, *Appl. Phys. Lett.* 92 (10) (2008) 104107.
- [10] S. Kawasaki, K. Nakatsuji, J. Yoshinobu, F. Komori, R. Takahashi, M. Lippmaa, K. Mase, A. Kudo, Epitaxial Rh-doped SrTiO₃ thin film photocathode for water splitting under visible light irradiation, *Appl. Phys. Lett.* 101 (3) (2012) 033910.
- [11] K. Furuhashi, Q. Jia, A. Kudo, H. Onishi, Time-resolved infrared absorption study of SrTiO₃ photocatalysts codoped with rhodium and antimony, *J. Phys. Chem. C* 117 (37) (2013) 19101–19106.
- [12] S. Ahmed, A. K.M. Sarwar Hossain Faysal, M. N.I. Khan, M. A. Basith, M.S. Bashir, H. N. Das, T. Hasan, I. Ahmed, Room temperature ferroic orders in Zr and (Zr, Ni) doped SrTiO₃, *Results Phys.* 31 (2021) 104940.
- [13] C. Franchini, Hybrid functionals applied to perovskites, *J. Phys. Condens. Matter* 26 (25) (2014) 253202.
- [14] S. Ahmed, S.S. Nishat, A. Kabir, A. K.M. Sarwar Hossain Faysal, T. Hasan, S. Chakraborty, I. Ahmed, Structural, elastic, vibrational, electronic and optical properties of SmFeO₃ using density functional theory, *Physica B Condens. Matter* 615 (2021) 413061.
- [15] A. Jain, Y. Shin, K.A. Persson, Computational predictions of energy materials using density functional theory, *Nat. Rev. Mater.* 1 (1) (2016) 1–13.
- [16] T. Liu, X. Zhou, M. Dupuis, C. Li, The nature of photogenerated charge separation among different crystal facets of BiVO₄ studied by density functional theory, *Phys. Chem. Chem. Phys.* 17 (36) (2015) 23503–23510.
- [17] T. Liu, Q. Zhao, C. Li, Y. Lyu, M. Dupuis, Photocatalytic facet selectivity in BiVO₄ nanoparticles: Polaron electronic structure and thermodynamic stability considerations for photocatalysis, *J. Phys. Chem. C* 123 (33) (2019) 20142–20151.
- [18] H.S. Park, K.E. Kweon, H. Ye, E. Paek, G.S. Hwang, A.J. Bard, Factors in the metal doping of BiVO₄ for improved photoelectrocatalytic activity as studied by scanning electrochemical microscopy and first-principles density-functional calculation, *J. Phys. Chem. C* 115 (36) (2011) 17870–17879.
- [19] J. Fardush Tanha, S. F.U. Farhad, U. Honey, N. I. Tanvir, T. Hasan, S. Shahriyar Nishat, A. Kabir, S. Ahmed, M. Hakim, M. N.I. Khan, M. Moniruzzaman, I. Ahmed, A DFT+U look into experimentally synthesized monoclinic scheelite BiVO₄, *J. Appl. Phys.* 130 (23) (2021) 235107.
- [20] J.Y. Zhang, J. Hwang, S. Raghavan, S. Stemmer, Symmetry lowering in extreme-electron-density perovskite quantum wells, *Phys. Rev. Lett.* 110 (25) (2013) 256401.
- [21] D.G. Ouellette, P. Moetakef, T.A. Cain, J.Y. Zhang, S. Stemmer, D. Emin, S.J. Allen, High-density two-dimensional small polaron gas in a delta-doped mott insulator, *Sci. Rep.* 3 (1) (2013) 1–5.
- [22] L. Bjaalie, A. Janotti, B. Himmetoglu, C. Van de Walle, Turning SrTiO₃ into a Mott insulator, *Phys. Rev. B* 90 (19) (2014) 195117.
- [23] C. Ricca, I. Timrov, M. Cococcioni, N. Marzari, U. Aschauer, Self-consistent site-dependent DFT+U study of stoichiometric and defective SrMnO₃, *Phys. Rev. B* 99 (9) (2019) 094102.
- [24] C. Ricca, I. Timrov, M. Cococcioni, N. Marzari, U. Aschauer, Self-consistent DFT+U+V study of oxygen vacancies in SrTiO₃, *Phys. Rev. Res.* 2 (2) (2020) 023313.
- [25] B. Lee, K.M. Choi, H.-S. Ahn, S. Han, J. Lee, et al., Oxygen vacancy clustering and electron localization in oxygen-deficient SrTiO₃: LDA+U study, *Phys. Rev. Lett.* 98 (11) (2007) 115503.
- [26] T. Xu, T. Shimada, M. Mori, G. Fujimoto, J. Wang, T. Kitamura, Defect engineering for nontrivial multiferroic orders in SrTiO₃, *Phys. Rev. Mater.* 4 (12) (2020) 124405.
- [27] Y. Zhang, J. Hu, E. Cao, L. Sun, H. Qin, Vacancy induced magnetism in SrTiO₃, *J. Magn. Magn.* 324 (10) (2012) 1770–1775.
- [28] J.U. Rehman, M.A. Rehman, M.B. Tahir, A. Hussain, T. Iqbal, M. Sagir, M. Usman, I. Kebaili, H. Alrobei, M. Alzaid, Electronic and optical properties of nitrogen and sulfur doped strontium titanate as efficient photocatalyst for water splitting: A DFT study, *Int. J. Hydrog. Energy* 47 (3) (2022) 1605–1612.
- [29] H.O. Jeschke, J. Shen, R. Valentí, Localized versus itinerant states created by multiple oxygen vacancies in SrTiO₃, *New J. Phys.* 17 (2) (2015) 023034.
- [30] P. Liu, J. Nisar, B. Pathak, R. Ahuja, Hybrid density functional study on SrTiO₃ for visible light photocatalysis, *Int. J. Hydrog. Energy* 37 (16) (2012) 11611–11617.
- [31] Q. Wang, T. Hisatomi, S.S.K. Ma, Y. Li, K. Domen, Core/shell structured La- and Rh-codoped SrTiO₃ as a hydrogen evolution photocatalyst in Z-scheme overall water splitting under visible light irradiation, *Chem. Mater.* 26 (14) (2014) 4144–4150.
- [32] M. Miyauchi, M. Takashio, H. Tobimatsu, Photocatalytic activity of SrTiO₃ codoped with nitrogen and lanthanum under visible light illumination, *Langmuir* 20 (1) (2004) 232–236.
- [33] W. Wei, Y. Dai, M. Guo, L. Yu, B. Huang, Density functional characterization of the electronic structure and optical properties of N-doped, and N/La-codoped SrTiO₃, *J. Phys. Chem. C* 113 (33) (2009) 15046–15050.
- [34] S. Tonda, S. Kumar, O. Anjaneyulu, V. Shanker, Synthesis of Cr and La-codoped SrTiO₃ nanoparticles for enhanced photocatalytic performance under sunlight irradiation, *Phys. Chem. Chem. Phys.* 16 (43) (2014) 23819–23828.
- [35] Y. Nakano, T. Morikawa, T. Ohwaki, Y. Taga, Origin of visible-light sensitivity in N-doped TiO₂ films, *Chem. Phys.* 339 (1–3) (2007) 20–26.
- [36] M. Batzill, E.H. Morales, U. Diebold, Influence of nitrogen doping on the defect formation and surface properties of TiO₂ rutile and anatase, *Phys. Rev. Lett.* 96 (2) (2006) 026103.
- [37] A. Okazaki, M. Kawaminami, Lattice constant of strontium titanate at low temperatures, *Mater. Res. Bull.* 8 (5) (1973) 545–550.
- [38] A. Janotti, B. Jalan, S. Stemmer, C.G. Van de Walle, Effects of doping on the lattice parameter of SrTiO₃, *Appl. Phys. Lett.* 100 (26) (2012) 262104.
- [39] Y.-L. Liu, C.-L. Yang, M.-S. Wang, X.-G. Ma, Y.-G. Yi, Theoretical insight into the effect of Si-doped sites on the photocatalytic properties of SrTiO₃, *Appl. Phys. A* 125 (6) (2019) 1–9.
- [40] G. Kresse, J. Furthmüller, Efficient iterative schemes for ab initio total-energy calculations using a plane-wave basis set, *Phys. Rev. B* 54 (16) (1996) 11169.
- [41] G. Kresse, D. Joubert, From ultrasoft pseudopotentials to the projector augmented-wave method, *Phys. Rev. B* 59 (3) (1999) 1758.
- [42] R.O. Jones, Density functional theory: Its origins, rise to prominence, and future, *Rev. Modern Phys.* 87 (3) (2015) 897.
- [43] W. Kohn, L.J. Sham, Self-consistent equations including exchange and correlation effects, *Phys. Rev.* 140 (4A) (1965) A1133.
- [44] J.P. Perdew, K. Burke, M. Ernzerhof, Generalized gradient approximation made simple, *Phys. Rev. Lett.* 77 (18) (1996) 3865.
- [45] S. Dudarev, G. Botton, S. Savrasov, C. Humphreys, A. Sutton, Electron-energy-loss spectra and the structural stability of nickel oxide: An LSDA+U study, *Phys. Rev. B* 57 (3) (1998) 1505.

- [46] V.I. Anisimov, J. Zaanen, O.K. Andersen, Band theory and Mott insulators: Hubbard U instead of stoner I, *Phys. Rev. B* 44 (3) (1991) 943.
- [47] J. Heyd, G.E. Scuseria, M. Ernzerhof, Hybrid functionals based on a screened Coulomb potential, *J. Chem. Phys.* 118 (18) (2003) 8207–8215.
- [48] A.V. Krukau, O.A. Vydrov, A.F. Izmaylov, G.E. Scuseria, Influence of the exchange screening parameter on the performance of screened hybrid functionals, *J. Chem. Phys.* 125 (22) (2006) 224106.
- [49] J. Paier, M. Marsman, K. Hummer, G. Kresse, I.C. Gerber, J.G. Ángyán, Screened hybrid density functionals applied to solids, *J. Chem. Phys.* 124 (15) (2006) 154709.
- [50] J. Paier, M. Marsman, G. Kresse, Dielectric properties and excitons for extended systems from hybrid functionals, *Phys. Rev. B* 78 (12) (2008) 121201.
- [51] J.P. Perdew, M. Ernzerhof, K. Burke, Rationale for mixing exact exchange with density functional approximations, *J. Chem. Phys.* 105 (22) (1996) 9982–9985.
- [52] A.D. Becke, A new mixing of Hartree-Fock and local density-functional theories, *J. Chem. Phys.* 98 (2) (1993) 1372–1377.
- [53] B.G. Janesko, T.M. Henderson, G.E. Scuseria, Screened hybrid density functionals for solid-state chemistry and physics, *Phys. Chem. Chem. Phys.* 11 (3) (2009) 443–454.
- [54] A. Stroppa, G. Kresse, Unraveling the Jahn-Teller effect in Mn-doped GaN using the Heyd-Scuseria-Ernzerhof hybrid functional, *Phys. Rev. B* 79 (20) (2009) 201201.
- [55] M. Marsman, J. Paier, A. Stroppa, G. Kresse, Hybrid functionals applied to extended systems, *J. Phys. Condens. Matter.* 20 (6) (2008) 064201.
- [56] A. Stroppa, S. Picozzi, Hybrid functional study of proper and improper multiferroics, *Phys. Chem. Chem. Phys.* 12 (20) (2010) 5405–5416.
- [57] A.A. Mostofi, J.R. Yates, Y.-S. Lee, I. Souza, D. Vanderbilt, N. Marzari, Wannier90: A tool for obtaining maximally-localised Wannier functions, *Comput. Phys. Comm.* 178 (9) (2008) 685–699.
- [58] J.P. Perdew, W. Yang, K. Burke, Z. Yang, E.K. Gross, M. Scheffler, G.E. Scuseria, T.M. Henderson, I.Y. Zhang, A. Ruzsinszky, et al., Understanding band gaps of solids in generalized Kohn-Sham theory, *Proc. Natl. Acad. Sci. USA* 114 (11) (2017) 2801–2806.
- [59] J.P. Perdew, M. Levy, Physical content of the exact Kohn-Sham orbital energies: band gaps and derivative discontinuities, *Phys. Rev. Lett.* 51 (20) (1983) 1884.
- [60] L.J. Sham, M. Schlüter, Density-functional theory of the energy gap, *Phys. Rev. Lett.* 51 (20) (1983) 1888.
- [61] H. Xiao, J. Tahir-Kheli, I.W.A. Goddard, Accurate band gaps for semiconductors from density functional theory, *J. Phys. Chem. Lett.* 2 (3) (2011) 212–217.
- [62] M. Arroyo-de Dompablo, A. Morales-García, M. Taravillo, DFT+U calculations of crystal lattice, electronic structure, and phase stability under pressure of TiO₂ polymorphs, *J. Chem. Phys.* 135 (5) (2011) 054503.
- [63] M. Fox, Optical properties of solids, 2002.
- [64] M. Dresselhaus, G. Dresselhaus, S.B. Cronin, A.G. Souza Filho, *Solid State Properties*, Springer, 2018.
- [65] I. Merad Boudia, A. Reshak, T. Ouahrani, Z. Bentalha, Density functional theory calculation of the optical properties and topological analysis of the electron density of MBi₂B₂O₇ (M=Ca, Zn) compounds, *J. Appl. Phys.* 113 (8) (2013) 083505.
- [66] T. Ouahrani, A.H. Reshak, A.O. de La Roza, M. Mebrouki, V. Luaña, R. Khenata, B. Amrani, First-principles study of structural, electronic, linear and nonlinear optical properties of Ga₂Psb ternary chalcopyrite, *Eur. Phys. J. B* 72 (3) (2009) 361–366.
- [67] A.H. Reshak, X. Chen, I. Kityk, S. Auluck, Specific features of second order optical susceptibilities for a complex borate crystal Bi₂ZnB₂O₇: Experiment and theory, *Curr. Opin. Solid State Mater. Sci.* 11 (3–4) (2007) 33–39.
- [68] R. Bell, G. Rupprecht, Elastic constants of strontium titanate, *Phys. Rev.* 129 (1) (1963) 90.
- [69] A. Beattie, G. Samara, Pressure dependence of the elastic constants of SrTiO₃, *J. Appl. Phys.* 42 (6) (1971) 2376–2381.
- [70] P.S. Narayanan, K. Vedam, Raman spectrum of strontium titanate, *Z. Phys.* 163 (2) (1961) 158–164.
- [71] W.G. Nilsen, J.G. Skinner, Raman spectrum of strontium titanate, *J. Chem. Phys.* 48 (5) (1968) 2240–2248.
- [72] R.F. Schaufele, M.J. Weber, First-and second-order raman scattering of SrTiO₃, *J. Chem. Phys.* 46 (7) (1967) 2859–2861.
- [73] C.H. Perry, J.H. Fertel, T.F. McNelly, Temperature dependence of the Raman spectrum of SrTiO₃ and KTiO₃, *J. Chem. Phys.* 47 (5) (1967) 1619–1625.
- [74] A.A. Sirenko, I.A. Akimov, J.R. Fox, A.M. Clark, H.-C. Li, W. Si, X.X. Xi, Observation of the first-order Raman scattering in SrTiO₃ thin films, *Phys. Rev. Lett.* 82 (22) (1999) 4500.
- [75] V. Lemanov, Concentration dependence of phonon mode frequencies and the Grüneisen coefficients in Ba_xSr_{1-x}TiO₃ solid solutions, *Phys. Solid State* 39 (2) (1997) 318–322.
- [76] X. Wu, D. Wu, X. Liu, Negative pressure effects in SrTiO₃ nanoparticles investigated by Raman spectroscopy, *Solid State Commun.* 145 (5–6) (2008) 255–258.
- [77] M. Muralidharan, V. Anbarasu, A.E. Perumal, K. Sivakumar, Carrier induced ferromagnetism in Yb doped SrTiO₃ perovskite system, *J. Mater. Sci. Mater.* 25 (9) (2014) 4078–4087.
- [78] U.D. Venkateswaran, V.M. Naik, R. Naik, High-pressure Raman studies of polycrystalline BaTiO₃, *Phys. Rev. B* 58 (21) (1998) 14256.
- [79] D. Tenne, I. Gonenli, A. Soukiassian, D. Schlom, S. Nakhmanson, K. Rabe, X. Xi, Raman study of oxygen reduced and re-oxidized strontium titanate, *Phys. Rev. B* 76 (2) (2007) 024303.
- [80] Y. Wang, J.E. Saal, Z. Mei, P. Wu, J. Wang, S. Shang, Z.-K. Liu, L.-Q. Chen, A first-principles scheme to phonons of high temperature phase: No imaginary modes for cubic SrTiO₃, *Appl. Phys. Lett.* 97 (16) (2010) 162907.
- [81] M. Cardona, Optical properties and band structure of SrTiO₃ and BaTiO₃, *Phys. Rev.* 140 (2A) (1965) A651.
- [82] X. Wu, D. Vanderbilt, D. Hamann, Systematic treatment of displacements, strains, and electric fields in density-functional perturbation theory, *Phys. Rev. B* 72 (3) (2005) 035105.
- [83] S. Shang, Y. Wang, Z.-K. Liu, First-principles elastic constants of α - and θ -Al₂O₃, *Appl. Phys. Lett.* 90 (10) (2007) 101909.
- [84] F. Mouhat, F.-X. Coudert, Necessary and sufficient elastic stability conditions in various crystal systems, *Phys. Rev. B* 90 (22) (2014) 224104.
- [85] M. Jamal, S.J. Asadabadi, I. Ahmad, H.R. Aliabad, Elastic constants of cubic crystals, *Comput. Mater. Sci.* 95 (2014) 592–599.
- [86] R. Hill, The elastic behaviour of a crystalline aggregate, *Proc. Phys. Soc. A* 65 (5) (1952) 349.
- [87] H. Dong, C. Chen, S. Wang, W. Duan, J. Li, Elastic properties of tetragonal BiFeO₃ from first-principles calculations, *Appl. Phys. Lett.* 102 (18) (2013) 182905.
- [88] M. Yaakob, M. Taib, M. Deni, A. Chandra, L. Lu, M. Yahya, First principle study on structural, elastic and electronic properties of cubic BiFeO₃, *Ceram. Int.* 39 (2013) S283–S286.
- [89] S.H. Simon, *The Oxford Solid State Basics*, OUP Oxford, 2013.
- [90] S. Baroni, S. De Gironcoli, A. Dal Corso, P. Giannozzi, Phonons and related crystal properties from density-functional perturbation theory, *Rev. Modern Phys.* 73 (2) (2001) 515.
- [91] F. Giustino, Electron-phonon interactions from first principles, *Rev. Modern Phys.* 89 (1) (2017) 015003.
- [92] S.-G. Ma, T. Gao, S.-C. Li, X.-J. Ma, Y.-H. Shen, T.-C. Lu, Theoretical investigations on the α -LiAlO₂ properties via first-principles calculation, *Fusion Eng. Des.* 113 (2016) 324–330.
- [93] W. Zhong, R. King-Smith, D. Vanderbilt, Giant LO-TO splittings in perovskite ferroelectrics, *Phys. Rev. Lett.* 72 (22) (1994) 3618.
- [94] L. Xie, J. Zhu, The electronic structures, Born effective charges, and interatomic force constants in BaMO₃ (M=Ti, Zr, Hf, Sn): A comparative first-principles study, *J. Am. Ceram. Soc.* 95 (11) (2012) 3597–3604.
- [95] P. Ghosez, J.-P. Michenaud, X. Gonze, Dynamical atomic charges: The case of ABiO₃ compounds, *Phys. Rev. B* 58 (10) (1998) 6224.
- [96] P. Ghosez, X. Gonze, P. Lambin, J.-P. Michenaud, Born effective charges of barium titanate: Band-by-band decomposition and sensitivity to structural features, *Phys. Rev. B* 51 (10) (1995) 6765.
- [97] S. Shah, P. Bristowe, A. Kolpak, A. Rappe, First principles study of three-component SrTiO₃/BaTiO₃/PbTiO₃ ferroelectric superlattices, *J. Mater. Sci. Mater.* 43 (11) (2008) 3750–3760.
- [98] W.A. Harrison, *Electronic Structure and the Properties of Solids: The Physics of the Chemical Bond*, Courier Corporation, 2012.
- [99] L.F. Mattheiss, Energy bands for KNiF₃, SrTiO₃, KMoO₃, and KTaO₃, *Phys. Rev. B* 6 (12) (1972) 4718.
- [100] C.E. Ekuma, M. Jarrell, J. Moreno, D. Bagayoko, First principle electronic, structural, elastic, and optical properties of strontium titanate, *AIP Adv.* 2 (1) (2012) 012189.
- [101] M. Marques, L. Teles, V. Anjos, L. Scalfaro, J. Leite, V. Freire, G. Farias, E. da Silva Jr., Full-relativistic calculations of the SrTiO₃ carrier effective masses and complex dielectric function, *Appl. Phys. Lett.* 82 (18) (2003) 3074–3076.
- [102] W. Wunderlich, H. Ohta, K. Koumoto, Enhanced effective mass in doped SrTiO₃ and related perovskites, *Phys. B Condens. Matter* 404 (16) (2009) 2202–2212.